Geophysical Journal International

Geophys. J. Int. (2026) **244,** 1–16
https://doi.org/10.1093/gji/ggaf507
Advance Access publication 2025 December 11
Research Paper

Static and quasi-static inversion of fault slip during laboratory earthquakes

F. Arzu, C. Twardzik, B. Fryer, Y. Xie, J.-P. Ampuero and F. Passelègue
Université Côte d'Azur , Observatoire de la Côte d'Azur, Géoazur, CNRS, Sophia-Antipolis, 06560, *Valbonne, France. E-mail: feyza.arzu@geoazur.unice.fr*

Accepted 2025 December 8. Received 2025 December 5; in original form 2025 August 8

SUMMARY

Inferring the spatiotemporal distribution of slip during earthquakes remains a significant challenge due to the high dimensionality and ill-posed nature of the inverse problem. As a result, finite-source inversions typically rely on simplified assumptions. Moreover, in the absence of ground-truth measurements, the performance of inversion methods can only be evaluated through synthetic tests. Laboratory earthquakes offer a valuable alternative by providing 'simulated real data' and ground truth observations under controlled conditions, enabling a more reliable evaluation of source inversion procedures. In this study, we present static and quasi-static slip inversion results from data recorded during laboratory earthquakes. Each event is instrumented with 20 accelerometers along the fault, and the recorded acceleration data are used to invert for the slip history. We consider two different types of Green's functions (**GF**): simplistic **GF** assuming a homogeneous elastic half-space and realistic **GF** computed by finite element modelling of the experimental setup. The inversion results are then compared to direct observations of fault slip and rupture velocity obtained independently during the experiments. Our results show that, regardless of the **GF** used, the inversions fit well with the data and result in small formal uncertainties of model parameters. However, only the inversion with realistic **GF** yields slip distributions consistent with the true fault slip measurements and successfully recovers the distribution of rupture velocity along the fault. These findings emphasize the critical role of **GF** selection in accurately resolving slip dynamics and highlight an important distinction in Bayesian inversion: while posterior uncertainty quantification is essential, it does not guarantee accuracy, especially if forward modelling uncertainties are not properly accounted for. Thus, confidence in inversion results must be paired with careful modelling choices to ensure physical reliability.

Key words: Bayesian inference; Finite element method; Inverse theory; Monte Carlo methods; Earthquake ground motions; Earthquake source observations.

1 INTRODUCTION

Estimating the spatial and temporal evolution of slip during earthquakes is essential to understand the physics that controls the seismic cycle (J.P. Avouac 2015; P.M. Mai *et al.* 2016; Z. Duputel 2022). The behaviour of faults is strongly influenced by their complex structure and interactions with the surrounding environment. Faults are not smooth or linear but rather rough, segmented and intricate (Y. Ben-Zion & C.G. Sammis 2003), which affects their frictional properties (C. Scholz 2002) and determines whether slip is seismic or aseismic (R. Sibson 1989). Moreover, faults are not isolated; they interact with one another, sometimes triggering sequences of earthquakes presenting different seismic behaviours (P. Romanet *et al.* 2018). Since fault slip occurs at depth, direct *in-situ* measurements are impossible, and estimates of fault slip histories are inferred from remote observations, usually recorded at the surface, by solving an inverse problem (A. Tarantola & B. Valette 1982). Therefore, our understanding of earthquake physics is limited by the data set used to invert for slip history, as well as the assumptions about the forward problem (P.C. Hansen 1998; I.A. Beresnev 2003; S. Hartzell *et al.* 2007; P.M. Mai *et al.* 2016).

In finite-fault inversions, one of the largest sources of uncertainty arises from the inaccuracy of the Green's functions (**GF**), due to uncertainty about the fault geometry or the medium properties (Y. Yagi & Y. Fukahata 2008; S. Minson *et al.* 2013; Z. Duputel *et al.* 2014, 2015; T. Ragon *et al.* 2018; M. Hallo & F. Gallovič 2020; F. Ortega-Culaciati *et al.* 2021). Additionally, the problem is most often ill-posed, meaning multiple models can explain the observations equally well (e.g. P.C. Hansen 1998; E. Clévédé *et al.* 2004; J.W.C. Wong *et al.* 2024), making it difficult to infer the true solution. Ill-posedness is commonly addressed by solving the inverse problem using regularization, which can result in biased results (F.

Gallovič & J. Zahradník 2011; F. Gallovič & J.P. Ampuero 2015; F. Ortega-Culaciati *et al.* 2021).

In problems where the solution is non-unique, it is important to explore the range of admissible solutions rather than seeking a single best fit. This can be approached through optimization-based techniques or probabilistic frameworks. Among these, Bayesian inversion methods estimate the posterior probability density function of the model parameters by combining prior knowledge with the likelihood of the observations for a given model. In practice, this is done by sampling the model parameter space and obtaining multiple solutions that are compatible with the observations (e.g. A. Tarantola 2005; S. Minson *et al.* 2013). Posterior distributions allow for the estimation of parameter uncertainties and the identification of the most probable solutions, thereby enhancing the reliability of the interpretations derived from the models. However, the quantification of posterior model uncertainties does not necessarily guarantee the accuracy of the solution (e.g. P.M. Mai *et al.* 2016; C. Twardzik *et al.* 2022), especially if modelling assumptions, like the Green's functions, are inaccurate.

To address these concerns, synthetic tests are usually employed (e.g. R.W. Graves & D.J. Wald 2001; T. Okamoto & H. Takenaka 2009; Z. Duputel *et al.* 2014; M. Hallo & F. Gallovič 2020; F. Ortega-Culaciati *et al.* 2021; L. Langer *et al.* 2022). These studies note that good data fitting with an imperfect **GF** does not necessarily guarantee an accurate solution. In some synthetic tests, this is exposed by generating data using a prescribed (ground-truth) source and a prescribed **GF**, while doing the source inversion assuming a different **GF**. While these approaches provide useful information on the capabilities and limitations of the source inversion procedure, they typically rely on overly simplified source models. Laboratory earthquakes provide a valuable alternative to synthetic tests because they exhibit greater complexity and variability in rupture behaviour, which better reflects the diversity seen in natural earthquakes. At the same time, laboratory experiments are conducted in a well-known and controlled medium; they reduce the epistemic uncertainties such as fault geometry and material properties, which affect **GF** calculations (T. Okamoto & H. Takenaka 2009; L. Langer *et al.* 2022) and inferred slip models (Y. Yagi & Y. Fukahata 2008; S. Minson *et al.* 2013; Z. Duputel *et al.* 2014; T. Ragon *et al.* 2018). Despite these major advantages offered by studying laboratory earthquakes, attempts to apply source inversion methods to experimental data remain limited (P. Dublanchet *et al.* 2024).

In this paper, we study the ability to retrieve the spatiotemporal slip of laboratory earthquakes using displacement time-series obtained from accelerometers located along the fault. This is done within a Bayesian source inversion framework, which provides not just one solution but an ensemble of solutions enabling us to evaluate the uncertainty of the retrieved model parameters. First, we examine the inverse problem of retrieving the final slip distribution, hereafter called static slip inversion. In particular, we investigate how the choice of **GF** affects the reliability of the inferred slip distribution. To this end, we compare two different **GF** formulations: a simple **GF** based on analytical solutions for a homogeneous half-space medium (Y. Okada 1992) and a realistic **GF** based on numerical finite element modelling (COMSOL, Inc. 2024) of the experimental setup. The objective of this comparison is to quantify how inappropriate boundary condition assumptions affect the inversion results in our laboratory setup. Secondly, we investigate our ability to recover the rupture front by inverting for the spatiotemporal distribution of slip from near-field displacement time-series data with a static Green's function, hereafter called quasi-static slip inversion. This approach is similar to that of S.E. Minson *et al.* (2014), who inverted quasi-static offsets from high-rate GPS data to characterize the evolving rupture in real time.

2 EXPERIMENTAL PROTOCOL AND RESULTS

2.1 Experimental setup

Experiments were conducted using the biaxial apparatus, *Crakdyn*, housed at the Géoazur laboratory in Valbonne, France. The experimental fault is the contact surface between two rectangular polymethyl methacrylate (PMMA) blocks, measuring 40 × 10 × 1 cm^3 and 45 × 10 × 1.8 cm^3, respectively. The dimensions of the fault are 40 × 1 cm^2 (Fig. 1a).

A normal force, F_{N}, was applied using three independently controlled vertical pistons (F_{N_1}, F_{N_2} and F_{N_3}), while a shear force, F_{S}, was applied via a single horizontal piston. Each piston was equipped with a dedicated load cell recording at 500 Hz. Both normal and shear forces were manually regulated using Enerpac hydraulic pumps capable of achieving oil pressures up to 700 bar. Loading was applied incrementally in 30-bar steps, increasing both the nominal normal stress, σ^0, and the nominal shear stress, τ, at the pistons [the corresponding load cell records are shown in Figs 1(b) and (c)]. The loading phase terminated when σ^0 reached 120, 130, 140 or 150 bar at all vertical pistons, depending on the experiment, while τ reached 190 bar. Hence, the initial stress conditions of the fault vary as a function of nominal normal stress, such that as σ^0 increases, the initial stress ratio, f_0, decreases. Here, 'nominal stress' refers to the gauge pressure readings from the hydraulic system and does not directly correspond to the local or average stress along the fault interface. The load cell data provide a more accurate representation of average stress. Rupture was initiated by partially unloading the piston F_{N_3}, until triggering the first event of the experiment to have control over the rupture size (Figs 1b and c).

During rupture, particle accelerations were recorded using twenty Brüel & Kjær type 8309 accelerometers with a corner frequency of 56 kHz. These sensors recorded continuously at 2 MHz during the unloading phase. Thirteen accelerometers were oriented horizontally and seven vertically, positioned approximately 1 cm from the fault to preferentially measure fault-parallel and fault-perpendicular accelerations, respectively. Fault slip was measured using ten Philtec D100-E2H2PQT5 optical gap sensors placed across the fault. These sensors, with a 500 kHz cutoff frequency and a resolution of 0.4 microns, are capable of detecting slip up to 0.5 mm. Sampling was performed continuously at 2 MHz.

Dynamic rupture propagation was visualized using three high-intensity light sources to illuminate the sample. Transmitted light was recorded by a Phantom TMX 6410 high-speed camera, with cross-polarization achieved using two linear polarizing filters; one between the light sources and the sample and one between the sample and the camera. The camera was triggered via an oscilloscope connected to a piezoelectric sensor mounted on the sample. Images were captured at 500 kHz with a spatial resolution of 1280 × 32 pixels, corresponding to a pixel size of 312 microns. Because PMMA is birefringent, variations in transmitted light intensity correspond to changes in local stress, allowing for real-time tracking of rupture evolution using polarized imaging (A. Rosakis *et al.* 1999; S. Nielsen *et al.* 2010; A. Schubnel *et al.* 2011; S. Latour *et al.* 2013, 2024).

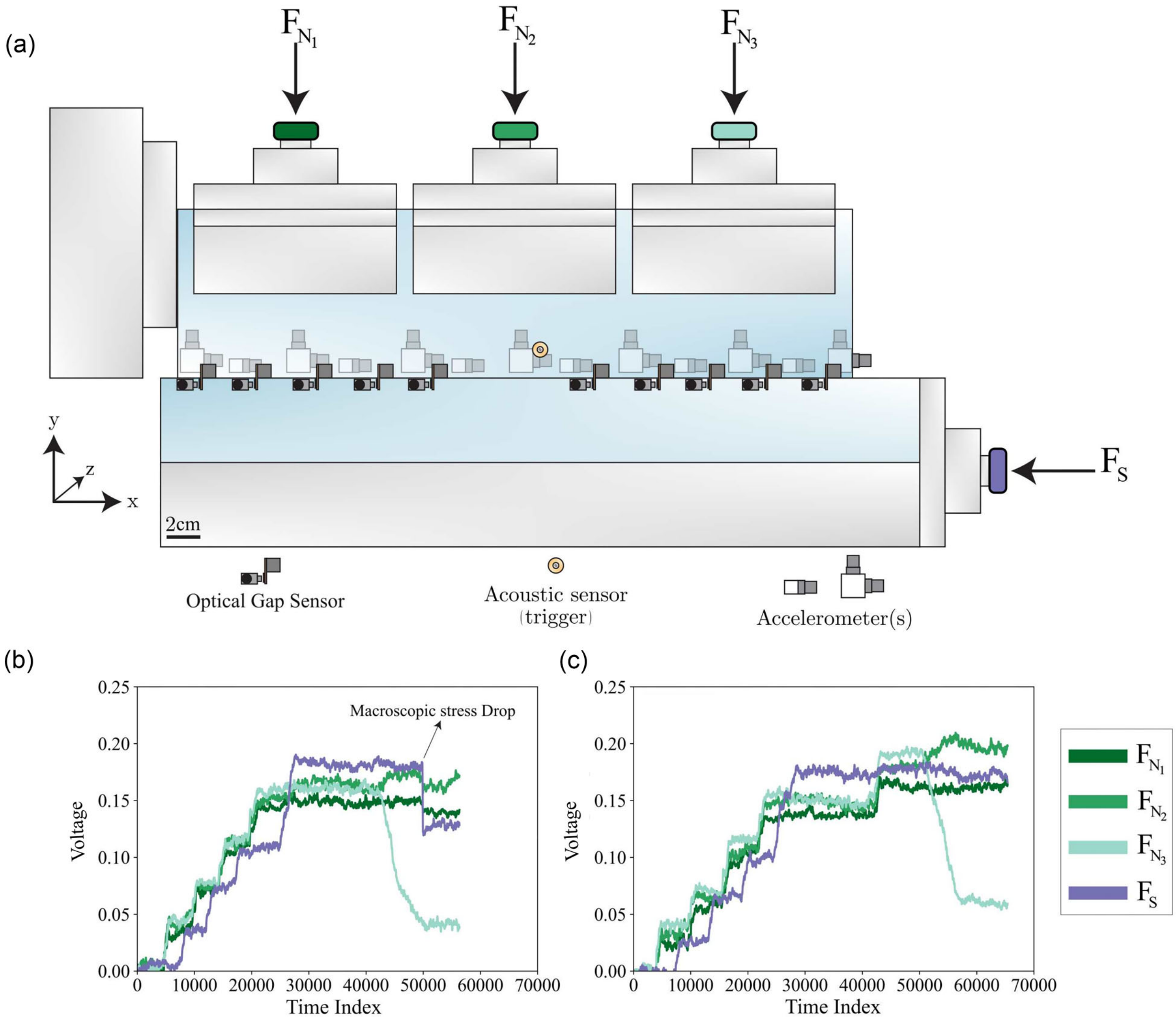

Figure 1. (a) Experimental setup. The contact surface between two PMMA plates form an experimental fault loaded in a biaxial apparatus. A normal load is applied via three independently controlled vertical pistons, F_{N_1}, F_{N_2} and F_{N_3}. A shear load is applied via a horizontal piston, F_S. Accelerometers and optical gap sensors are placed along the fault. A high-speed camera (not pictured) triggered by a piezoelectric sensor is used to track the rupture front. (b, c) Loading histories in two experiments: uncalibrated readings of the load cells used to record the applied normal loads and the shear load. (b) The normal and shear loads are increased in a step-wise manner until the fault is near criticality. Then, one normal piston is unloaded, triggering a dynamic event. Macroscopic stress drop occurs only in the case with the lowest nominal stress (highest initial stress ratio), indicating that the lack of normal stress barrier allows for complete rupture propagation (see B. Fryer *et al.* 2024). (c) Same procedure as (b), except a barrier is created by further increasing the normal load after criticality is initially reached.

2.2 Data processing

Optical gap sensors were calibrated such that a 5V output corresponded to the maximum displacement specified by the manufacturer. The number of operational gap sensors might change due to their sensitivity to alignment; some sensors may rotate or detach from the mounting surface during the experiment. Accelerometers were individually calibrated by Brüel & Kjær, enabling direct voltage-to-acceleration conversion. The acceleration instrument response is sufficiently flat over the frequencies relevant to the short rupture durations of our experiments. Displacement time-series at the accelerometer locations were obtained by double integration of the acceleration signals after removing the mean and linear trend; no filtering was applied. For high-speed imaging, the greyscale intensity of each pixel (ranging from black to white) reflects variations in transmitted light, which in turn relate to local stress changes (Fig. 2). A horizontal line of pixels close to the fault was extracted for 1-D spatial analysis. The mean greyscale value over the first 20 frames was used as a reference. As rupture propagated, evolving stress states altered pixel intensities, which were then compared to the reference to generate videograms illustrating rupture dynamics (e.g. Fig. 2).

2.3 Experimental results

We consider four experiments with different applied σ^0, previously described in B. Fryer *et al.* (2024). In all these experiments, dynamic rupture nucleated near the location of the partially unloaded piston (F_{N_3}, in Fig. 1). As all experiments were conducted under the same nominal shear stress of 190 bar, differences in rupture behaviour can be attributed to variations in nominal normal, which modify the initial fault criticality. The ratio of the initial stress ratio to

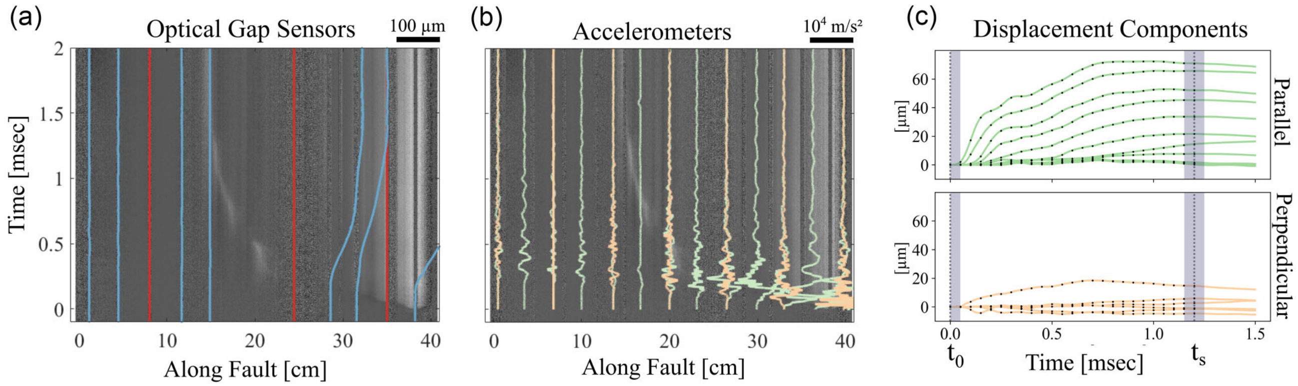

Figure 2. Results of an experiment with $\sigma^0 = 140$ bar. (a) Blue curves: time evolution of slip recorded by gap sensors; each trace is shifted to the sensor position. Red lines: gap sensors that were not operational during the experiment. Background greyscale: videogram showing the rupture propagation. (b) Green: fault-parallel acceleration. Orange: fault-perpendicular acceleration. Each trace is aligned to the sensor position, with positive acceleration to the right and negative to the left. (c) Green: fault-parallel displacement (obtained by integrating twice the acceleration records). Orange: fault-perpendicular displacement. t_0: slip onset; t_s: static end time. Grey shaded bands near t_0 and t_s indicate receiver noise and measurement error, respectively, used to obtain data covariance.

Table 1. Initial stress conditions.

σ^0	$\frac{f_0}{f_s}$
120	0.80
130	0.75
140	0.70
150	0.65

the static friction coefficient, f_0/f_s, provides a normalized measure of how close the initial stress condition lies to the peak strength of the fault. The static friction coefficient, f_s, is defined as the ratio between the shear force and the sum of the three individual normal forces measured at the onset of slip during regular friction experiments, without the unloading stage ($f_s \approx 0.5$). The initial stress ratio, f_0, is defined as the ratio between the shear force and the sum of the three individual normal forces measured on each piston immediately before initiating the unloading in Figs 1(b) and (c) that triggers rupture. These forces are measured directly by the load cells installed on the pistons. Although the stress distribution along the fault is heterogeneous, this force-based formulation provides a reasonable estimate of the overall loading conditions and allows consistent comparison between experiments.

As σ^0 increases, the ratio f_0/f_s decreases in Table 1, indicating that the fault is progressively farther from its peak strength. Load cell data show that events with higher-f_0, ($\sigma^0 = 120$ and 130 bar) exhibited clear macroscopic stress drops, whereas events with lower-f_0 ($\sigma^0 = 140$ and 150 bar) did not (Figs 1b and c). Videogram analysis (Fig. 3) revealed that higher-f_0 events propagated across the entire fault, indicating full rupture, while lower-f_0 events arrested mid-fault. Moreover, rupture velocities are slower for lower-f_0, even in events that reached the fault's end. The physical explanations of such changes in rupture properties were discussed in B. Fryer *et al.* (2024).

The time-series of true slip by the operational gap sensors confirm that slip only occurred at locations traversed by the rupture front (Fig. 2a). Acceleration amplitudes decreased from right to left, consistent with the direction of rupture propagation (Fig. 2b). Displacements derived from acceleration data served as input for subsequent slip inversion analyses (Fig. 2c).

3 RETRIEVING SLIP HISTORY FROM LABORATORY DISPLACEMENT DATA

Three ingredients are required to obtain the slip history during laboratory earthquakes: (1) observations of the rupture process, (2) a forward model that predicts observations given a prescribed source and (3) a procedure to search for models that generate predictions compatible with our observations. In this section, we describe our choices and settings for these three ingredients.

3.1 Observed data

To infer the laboratory earthquake rupture process, we use displacement time-series from the processing of accelerometer records, as explained in Section 2.2. These sensors record the motion of the PMMA block along only one direction. They are glued either parallel or perpendicular to the fault to capture both components of the acceleration (see Fig. 2c). The onset time, t_0 in Fig. 2(c), is manually selected just before the initiation of slip on the camera. The end time of the time-series, or static time, t_s, is also manually chosen as the moment when the displacement begins to plateau across all receivers. The values of t_s in Fig. 2(c) for the four experiments are 1.2, 1.3, 1.2 and 1.2 ms, respectively.

For the static inversion, that is when we aim to obtain only the final spatial slip distribution, the observations $\mathbf{d}_{\text{obs}}$ are defined as the total displacement cumulated at each receiver between t_0 and t_s, such that $\mathbf{d}_{\text{obs}} = \mathbf{u}(t_s) - \mathbf{u}(t_0)$, where $\mathbf{u}$ is the measured displacement (see Fig. 2c). The number of data points corresponds to the number of operational accelerometers and varies slightly between experiments due to occasional sensor failures: 18, 19, 18 and 19 operational accelerometers for the four experiments.

For the quasi-static slip inversion, that is, when we aim to obtain the spatiotemporal evolution of slip, the observations $\mathbf{d}_{\text{obs}}$ are the displacement time-series at each receiver. We downsample the time-series by a factor of 100 for computational efficiency. The resulting time-series used as data are shown as black dots in Fig. 2(c). The total number of observations is the number of receivers multiplied by the number of retained time-steps, resulting in data dimensions of:

$$18 \times 25, \quad 19 \times 27, \quad 18 \times 25, \quad 19 \times 25$$

for the four experiments as σ^0 increases, respectively.

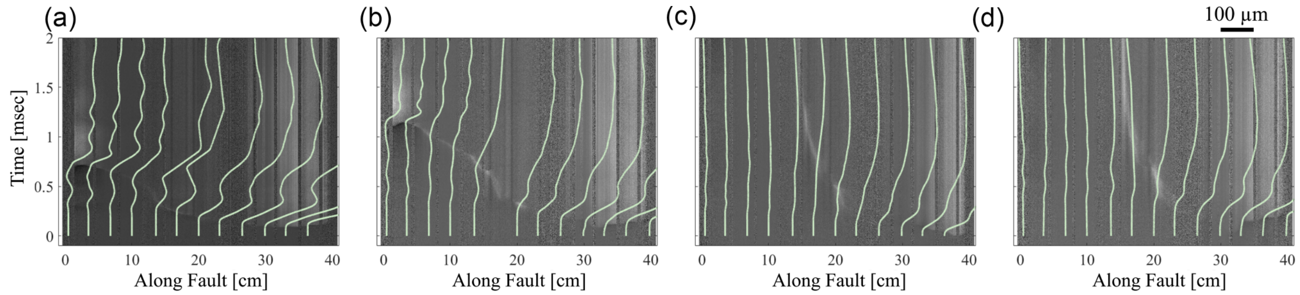

Figure 3. Local displacements (green curves) obtained by integrating acceleration signals that is placed in the receiver locations along the fault. (a) $\sigma^0 = 120$ bar, (b) $\sigma^0 = 130$ bar, (c) $\sigma^0 = 140$ bar, (d) $\sigma^0 = 150$ bar. The photoelasticity images in the background illustrate the evolution of rupture fronts.

3.2 Forward model: computing the Green's function of the medium

Both for static and quasi-static slip inversions, we assume a linear relation between the model parameters $\mathbf{m}$ describing fault slip and the predicted displacements $\mathbf{d}_{\mathrm{pred}}$, consistent with linear elasticity:

$$\mathbf{d}_{\mathrm{pred}} = \mathbf{G}\mathbf{m}, \tag{1}$$

where the matrix **G** collects the static **GF**s describing the elastic response of the medium to elementary sources.

The **GF**s are highly sensitive to the material properties and geometry of the medium, which are often heterogeneous and not fully constrained (e.g. T. Okamoto & H. Takenaka 2009; Z. Duputel *et al.* 2014; L. Langer *et al.* 2022). In addition, there are multiple ways to compute the **GF**, each based on different assumptions. While each has theoretical advantages and limitations, the choice of **GF** can introduce systematic biases into inversion results (F. Gallovič & J.P. Ampuero 2015; P.M. Mai *et al.* 2016). Therefore, selecting an appropriate formulation is critical but not always straightforward. In our case, we have a very good knowledge of the medium properties and the fault geometry. Therefore, we can focus on the differences that arise when we use a different formulation to calculate **G** in eq. (1). We compare two methods to compute displacements due to fault slip that differ in how they treat boundary conditions. The first approach uses the analytical solution by Y. Okada (1992) for the displacement field resulting from uniform slip on a rectangular patch (a rectangular dislocation) within a homogeneous elastic half-space. The second approach involves finite element simulations using the software COMSOL Multiphysics (COMSOL, Inc. 2024) and incorporating realistic features of the geometry and boundary conditions of the experimental setup (see Section A1 for details). The corresponding **G** matrices for these two approaches are hereafter denoted as $\mathbf{G}_{\mathbf{Ok}}$ and $\mathbf{G}_{\mathrm{Com}}$, respectively.

To make the computation in eq. (1) tractable, we discretize the model in both space and time. For spatial discretization, we simply subdivide the fault into a finite number of rectangular subfaults, where the slip distribution is assumed uniform for $\mathbf{G}_{\mathrm{Ok}}$ and tapered uniform for $\mathbf{G}_{\mathrm{Com}}$. The tapered nature of $\mathbf{G}_{\mathrm{Com}}$ will be discussed later in this section.

For the time discretization, we use the multi-time-windows method (A. H. Olson & R.J. Apsel 1982; S.H. Hartzell & T.H. Heaton 1983), in which slip can only occur within specific time intervals, each with a fixed duration. During each of these intervals, we describe the slip rate by a triangular basis function, as illustrated in Fig.4 By combining multiple basis functions, each delayed by its half-duration and properly weighted, we define the complete slip-rate function with the same time-step as the data set. We enforce positivity of the slip rate coefficients as a prior during sampling (details provided in Section 3.3). The time integral of such a slip-rate function yields a slip function that increases monotonically to the final slip value.

The optimal number of parameters is obtained by applying the Bayesian Information Criterion (see Section A2). The resulting number of unknown parameters is 10 for the static inversion (slip amplitude of 10 subfaults) and 80 for the quasi-static inversion (8 temporal basis function scaling coefficients for each of the 10 subfaults), as shown in Fig.A2 Thus, we have fewer model parameters (10 for static, 80 for quasi-static) than the number of data points ($\approx$ 20 for static, $\approx$ 500 for quasi-static), resulting in an overdetermined system.

In both **GF** approaches, we adopt the same values for fault geometry and material properties, which are well constrained. The fault is pre-defined, with strike and dip angles set to 90° for all subfaults. While the rake angle may vary slightly, we assume a constant rake of 180°, consistent with the right-lateral strike-slip motion inferred from the orientation of the accelerometer data. The medium is composed of PMMA, which behaves as a homogeneous, isotropic and linear elastic material under our experimental conditions. The *P*-wave velocity, v_{P}, *S*-wave velocity, v_{S} and density, ρ, have uniform values given in Table 2, from which we derive the Lamé parameters μ and λ.

$\mathbf{G}_{\mathrm{Ok}}$ appropriately represents natural faulting conditions, where a single free surface is present. In contrast, laboratory setup is surrounded by free surfaces. To assess the influence of the frontal and back free surfaces of the laboratory setup, we evaluated $\mathbf{G}_{\mathrm{Ok}}$ using both the actual fault width ($W = 1$ cm) and an infinitely large fault width ($W \gg L$). The latter mimics the effect of these two boundaries on the inverted slip distribution by preventing a saturation of slip imposed by fault width.

For $\mathbf{G}_{\mathrm{Com}}$, the finite element discretization employed quadratic Lagrange shape functions for the displacement field, corresponding to second-order elements with mid-edge nodes. For each subfault, a single simulation is performed by prescribing slip with an approximately uniform spatial slip distribution. To suppress boundary singularities, a symmetric half-cosine taper is applied along the two cross-strike edges of the rectangular subfaults. This ensures that the slip smoothly increases from zero to the prescribed uniform value and then decreases back to zero within a narrow margin of 0.01 cm in each subfault. A heterogeneous stress loading is considered in these simulations, with initial stress values listed in Table 3, to make sure the applied boundary conditions are meaningful. These values do not affect the result, as the **GF** represents the displacement field change resulting solely from fault slip.

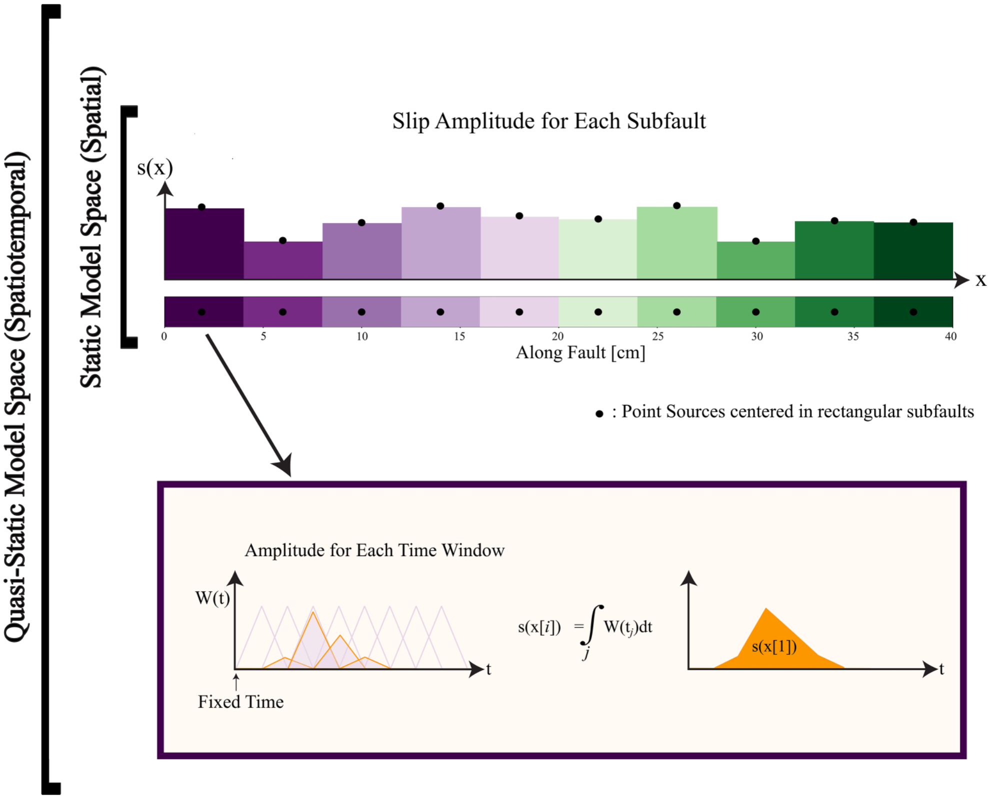

Figure 4. Parametrization of the source inversion problems. For spatial parametrization, the main fault is subdivided along strike into 10 rectangular subfaults. Each subfault is 4×1 cm^2 and has uniform slip. For time discretization, 8 triangular time basis functions for slip rate are defined in each subfault. The coefficient multiplying each time basis function, $W(t)$, is the contribution of the corresponding time interval to the total slip rate function.

Table 2. Material properties of PMMA

Parameter	**Value**	**Unit**
v_{P}	2700	m s^{-1}
v_{S}	1345	m s^{-1}
ρ	1100	kg m^{-3}
μ	$\rho \cdot v_{\text{S}}^2$	Pa
λ	$\rho \cdot v_{\text{P}}^2 - 2\rho \cdot v_{\text{S}}^2$	Pa

Table 3. Initial stress conditions for **GF** calculation in Comsol

The force variable on piston	**Applied stress value**
F_{N_1}	120 bar
F_{N_2}	120 bar
F_{N_3}	0 bar
F_S	190 bar

The displacements resulting from the two **GF** approaches differ significantly, as illustrated in Fig.5 The Okada solution produces nearly identical displacements for all subfaults, up to a lateral shift. This spatial invariance is a consequence of the idealized assumptions of a homogeneous elastic half-space. In contrast, the COMSOL solution exhibits notable spatial variability as a function of subfault location. This variation primarily arises from the presence of boundaries on the left and right sides of the experimental setup, and from differences in the thicknesses of the upper and lower PMMA blocks. Although the difference between the two **GF** displacements is minimal at very close distance to any given subfault, it increases substantially with distance from the source (Figs 5c and f). These results illustrate the strong sensitivity of Green's functions to assumptions about geometry and boundary conditions, emphasizing the need for careful modelling choices.

3.3 Bayesian approach

We perform our inversions using a Bayesian framework, in which the objective is to estimate the post-PDF of the slip model parameters, $\mathbf{m}$, conditioned on the observed displacement data, $\mathbf{d}_{\text{obs}}$. This relationship follows directly from Bayes' theorem:

$$p(\mathbf{m} \mid \mathbf{d}_{\text{obs}}) \propto p(\mathbf{m})\, p(\mathbf{d}_{\text{obs}} \mid \mathbf{m}), \tag{2}$$

where the prior distribution $p(\mathbf{m})$ is uniform: $\mathcal{U}(-10^{-4}, 500)\,\mu$m for the final slip in each subfault. The upper bound for slip is set to 500 μm, approximately five times the maximum observed fault-parallel displacement. The lower bound is slightly negative, because allowing a small negative range avoids this boundary effect and enables more efficient exploration of models with slip amplitudes close to zero. The likelihood function $p(\mathbf{d}_{\text{obs}} \mid \mathbf{m})$ is the probability that the observations $\mathbf{d}_{\text{obs}}$ are compatible with the model $\mathbf{m}$. This can be quantified by comparing the observations with the model's predictions while accounting for the uncertainties in the observations. We adopt a Laplacian distribution for the observation uncertainties:

$$p(\mathbf{d}_{\text{obs}} \mid \mathbf{m}) = \prod_{i=1}^{N} \frac{1}{\sqrt{2\mathrm{C}_d{}^{i}}} \exp\left(-\frac{\sqrt{2}}{\sqrt{\mathrm{C}_d{}^{i}}}\left|d_i^{\text{obs}} - d_i^{\text{pred}}\right|\right), \tag{3}$$

where $|\cdot|$ denotes the L_1 norm, and $\mathrm{C}_d{}^{i}$ is the square of the standard deviation of the uncertainty on the data derived from the i-th

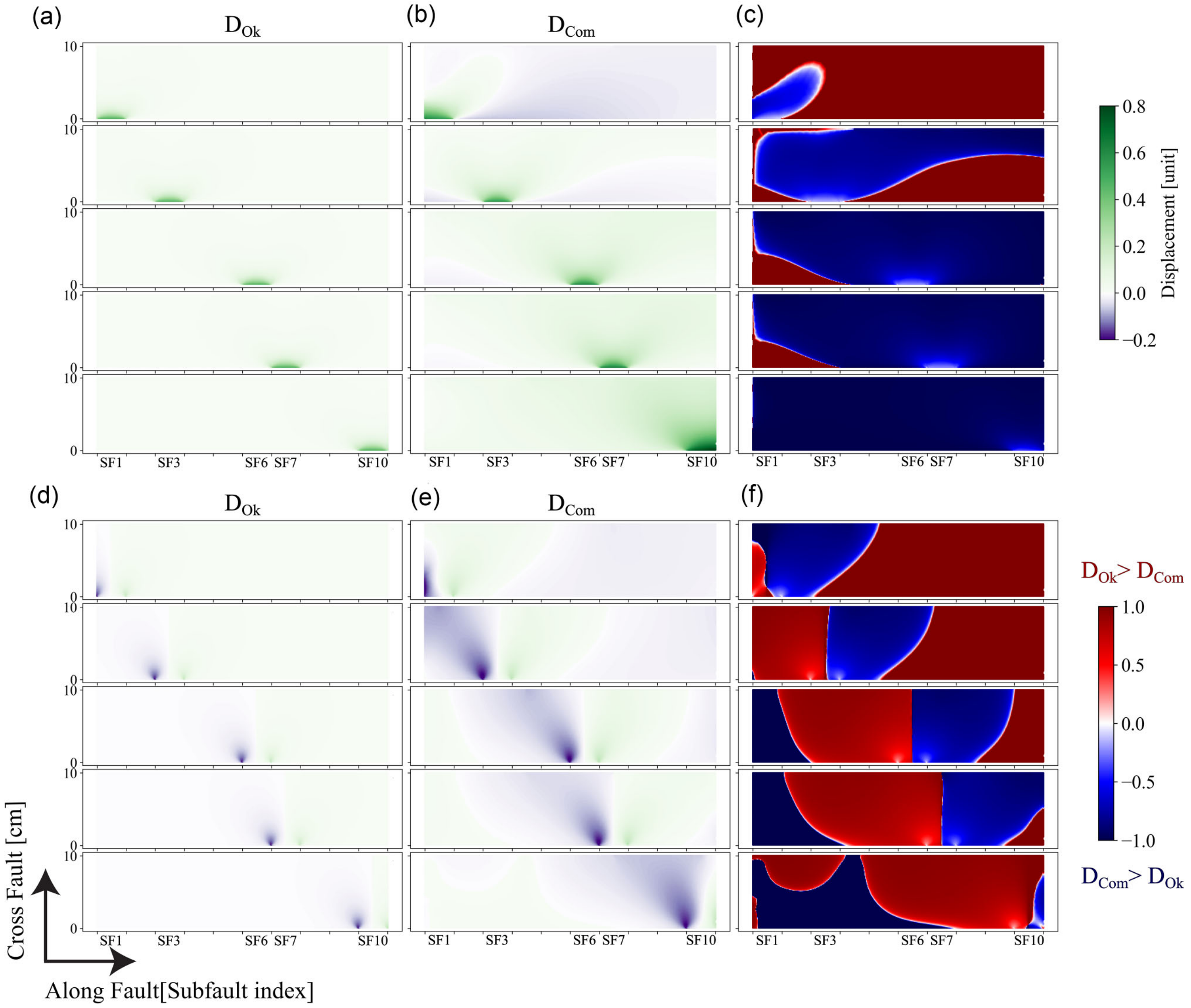

Figure 5. Fault-parallel (a, b) and fault-perpendicular (d, e) displacement fields, calculated for unit slip applied to five different 4 × 1 cm^2 rectangular subfaults, namely SF1, SF3, SF6, SF7, SF10, using $\mathbf{G}_{\mathrm{Ok}}$(a, d) and $\mathbf{G}_{\mathrm{Com}}$(b, e). (c, f) Relative differences $\frac{\mathrm{D}_{\mathrm{Ok}}-\mathrm{D}_{\mathrm{Com}}}{|\mathrm{D}_{\mathrm{Com}}|}$ for fault-parallel and fault-perpendicular displacements, respectively, where $\mathrm{D}_{\mathrm{Ok}} = \mathbf{G}_{\mathrm{Ok}}$(Unit slip) and $\mathrm{D}_{\mathrm{Com}} = \mathbf{G}_{\mathrm{Com}}$(Unit slip).

receiver. As explained in S.E. Minson & W.H.K. Lee (2014), this is equivalent to adopting a cost function based on the L_1 norm in optimization problems.

The data covariance C_d represents the uncertainty in the measured static displacement. To calculate this, we determine the variance of the displacement data in two windows of 100 data points, one immediately after t_0 (i.e., all data points until t_1 in the raw displacement data) and the other one immediately before and after t_s. These windows correspond to the shaded gray regions in Fig. 2(c). The former reflects the influence of background noise, whereas the latter accounts for measurement errors associated with identifying the final displacement. The two variances are then combined to represent the uncertainty of static displacement at each receiver.

We sample the posterior distribution by the Metropolis algorithm (W.K. Hastings 1970), which is a Markov Chain Monte Carlo (MCMC) method. This algorithm generates a sequence of samples by proposing candidate models, then accepting or rejecting them through a criterion based on the posterior probability. Over time, the sequence converges to the target distribution, allowing us to approximate the Bayesian solution effectively. We implement a straightforward Metropolis sampler (Z. Duputel 2024).

4 INVERSION RESULTS

4.1 Static inversion: comparison between Okada- and COMSOL-based GFs

In this section, we compare the static slip inversion results using the two **GFs** formulations, $\mathbf{G}_{\mathrm{Ok}}$ and $\mathbf{G}_{\mathrm{Com}}$, introduced in Section 3.2. We run a static inversion for each experiment. However, only the experiments conducted at $\sigma^0 = 140$ bars offered the possibility to confront our inversion results with the direct measurements of the fault slip recorded by the optical gap sensors. For the remaining experiments, the optical-gap sensors could not provide reliable slip measurements. During those runs, the laser beams were imperfectly aligned with their mirrors, leading to signal saturation and, ultimately, a faulty laser calibration. Because the resulting gap-sensor data are not trustworthy, we restrict the comparison between inversion results and direct slip observations to the experiment performed at $\sigma^0 = 140$ bars.

To mitigate sensitivity to the selected initial model, we run 100 independent MCMC chains, each initialized with a random model drawn from the prior distribution. Each chain consists of 10^5 steps and yields an acceptance rate of approximately 0.25 (A. Gelman *et al.* 1997). The convergence times depend on the choice of **GF**s, thus we have a different burn-in phase for each case. When using $\mathbf{G}_{\mathrm{Ok}}$, the first 20 per cent of each chain is discarded as burn-in. When using $\mathbf{G}_{\mathrm{Com}}$, the burn-in phase is 40 per cent. We also apply thinning by retaining only every 25th sample in each chain to promote independence between samples and to reduce the storage requirement. This results in 8×10^4 samples per chain and 2×10^6 slip models in total.

Figs 6(a) and (b) shows a comparison of the data fit when using $\mathbf{G}_{\mathrm{Ok}}$ and $\mathbf{G}_{\mathrm{Com}}$. We show the average of the predictions obtained from a set of randomly sampled slip models after the burning phase. Regardless of the **GF**s used, the inversions fit the data well (except for the perpendicular component at the receiver located at $x = 33$ cm, which is underestimated by both inversions). The root mean square error (RMSE) is 2.86 and 3.66 µm for the $\mathbf{G}_{\mathrm{Com}}$ and $\mathbf{G}_{\mathrm{Ok}}$ predictions, respectively, while the noise level of the observed data (standard deviation) is 0.69 µm. This indicates that both predictions are above the noise level, but $\mathbf{G}_{\mathrm{Com}}$ fits the data significantly better.

Figs 6(c) and (d) shows the average slip profiles and associated uncertainties derived from the posterior PDF for both inversions. Comparing the results with the ground truth reveals that the COMSOL-based inversion better reproduces the true slip profile. On the other hand, the Okada-based results, both for $W = 1$ cm and $W \gg L$, still deviate significantly. Although the $W \gg L$ assumption yields a better agreement with the true slip distribution than the $W = 1$ cm assumption, the improvement remains limited. Near $x = 33$ cm, where the model fit is poor, the COMSOL-based solution shows increased uncertainty, while the Okada-based solution with $W = 1$ cm exhibits unrealistically low uncertainty that does not encompass the true slip value. Moreover, the uncertainty associated with $\mathbf{G}_{\mathrm{Ok}}$ varies with boundary conditions: the $W = 1$ cm case yields negligible uncertainty, whereas the infinite-width case produces larger and more physically realistic uncertainty estimates.

To emphasize the advantage of the sampling algorithm, we compared the analytical and empirical model covariance matrices for both $\mathbf{G}_{\mathrm{Com}}$ and $\mathbf{G}_{\mathrm{Ok}}$. The empirical covariance matrix is obtained from the inferred posterior distributions, while the analytical one is derived under the Gaussian noise assumption in the data (Appendix A3). As shown in Fig. A3, $\mathbf{G}_{\mathrm{Com}}$ generally yields lower analytical covariances than $\mathbf{G}_{\mathrm{Ok}}$, whereas $\mathbf{G}_{\mathrm{Ok}}$ exhibits stronger diagonal dominance. Although this might suggest that $\mathbf{G}_{\mathrm{Com}}$ is more ill-posed, it captures the physics of the problem more accurately than $\mathbf{G}_{\mathrm{Ok}}$. For both **GF** formulations, the empirical model covariances are notably larger than the analytical ones. This discrepancy indicates that the linear-Gaussian framework underestimates the true model uncertainty, especially when the forward problem exhibits nonlinearities or the posterior distribution deviates from a Gaussian distribution.

4.2 Quasi-static inversion results using COMSOL-based GFs

To further challenge the robustness of our inversion methodology, we also perform quasi-static slip inversions for all four rupture events (Fig. 3). Since the static results presented above show a significant deviation of the slip amplitude from ground-truth measurements when using $\mathbf{G}_{\mathrm{Ok}}$, we do the quasi-static slip inversion only using $\mathbf{G}_{\mathrm{Com}}$. As outlined in Section 3.2, the model space is 80-dimensional for quasi-static inversion, which requires more samples for convergence than the static case. We run 100 independent MCMC chains with 10^6 samples each, discarding the first 20 per cent as burn-in and applying thinning by retaining every 25th sample.

The spatiotemporal slip distribution is obtained by taking the average of the posterior PDF (Figs 7a–d). The final time-step corresponds to the static slip distribution. As expected, decreasing the initial ratio τ_0/σ_n leads to reduced slip amplitudes and shorter rupture lengths (Figs 7a–d). Additionally, in the $\sigma^0 = 150$ bar experiment (Fig. 7d), slip starts later than in other experiments. This delay likely results from a foreshock that prematurely triggered the data acquisition system (Fig. 3d), highlighting the temporal sensitivity of the inversion method.

To obtain the spatiotemporal evolution of the rupture front from the quasi-static slip inversion, we define the rupture front by a slip amplitude threshold ranging from 1 per cent to 4 per cent of the maximum slip. These fronts are then compared with photoelastic observations (Figs 7e–h). The method retrieves rupture fronts, rupture velocities and features such as acceleration and deceleration. Minor timing discrepancies, especially at higher normal stress, arise from the use of finite slip thresholds to define rupture fronts: while true rupture onset corresponds to zero slip, thresholding introduces slight delays. Despite this, the inversion reliably recovers rupture propagation, length and nucleation location, with well-quantified uncertainty bounds.

For full ruptures (e.g. $\sigma^0 = 120$ and 130 bar), the inversion accurately captures the observed rupture propagation. For partial ruptures (e.g. $\sigma^0 = 140$ and 150 bar), it correctly identifies rupture arrest positions. However, resolution diminishes toward the rupture tip, where data sensitivity is inherently lower.

In the experiments conducted at $\sigma^0 = 120$ and 130 bar, rupture initiates on the right side of the fault, decelerates near $x = 17$ cm and subsequently re-accelerates along the left portion of the fault (Figs 7i and j). Such rupture complexities, namely the local deceleration and re-acceleration of the rupture front, have also been reported in previous studies (S.B.L. Cebry *et al.* 2023; F. Paglialunga *et al.* 2025). These behaviours are likely related to stress heterogeneities along the interface, possibly arising from the mechanical discontinuity between the metal components of the apparatus and the top PMMA block. Eventually, this asymmetric rupture evolution produces a two-stage slip pattern clearly resolved in the inversion results. The first slip phase occurs up to approximately $t = 0.75$ ms, followed by a brief interval of quiescence during which slip evolution stagnates. A second slip phase then starts and persists until around the final time-step t_s. Thus, the inversion can reveal rupture complexity, including transient pauses and rupture deceleration, consistent with experimental observations (Figs 7e–f). The narrow uncertainty bounds around the inferred fronts further support the robustness of rupture arrest detection, confirming that the slip did not progress beyond the indicated points at the applied thresholds (Figs 7i–l).

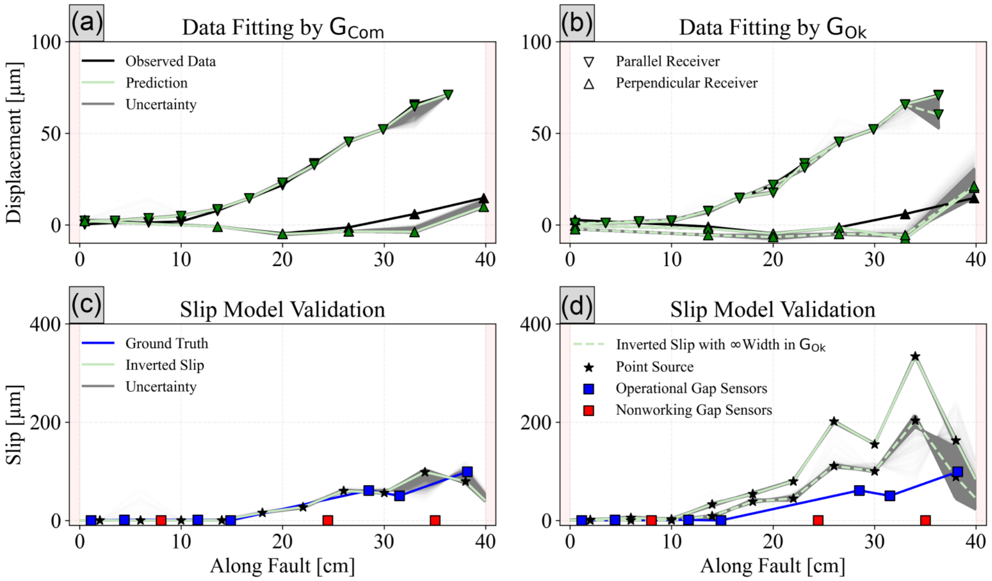

Figure 6. Comparison of static slip inversion results and their uncertainties using $\mathbf{G}_{\mathrm{Com}}$ and $\mathbf{G}_{\mathrm{Ok}}$. (a, b) Data fitting results using $\mathbf{G}_{\mathrm{Com}}$ and $\mathbf{G}_{\mathrm{Ok}}$ for fault-parallel (∇s) and fault-perpendicular (Δs) displacement components. (c, d) Comparison of inverted slip distributions with ground-truth slip data from gap sensors (blue and red rectangles indicate operational and non-operational sensors, respectively, so that blue curve is the ground truth). The dashed lines in (b, d) are data predictions and inverted model by $\mathbf{G}_{\mathrm{Ok}}$ with infinitely wide subfault assumption ($W \gg L$). Black stars denote the centres of subfaults. Light green curves represent linearly interpolated slip distributions between these subfault centres, based on the inverted slip model that is the average value of all collected slip models after burn-in phase. To estimate the uncertainty, we draw randomly 5000 samples from the posterior distribution that we have obtained from the MCMC inversion such that it illustrates the variability of the solutions.

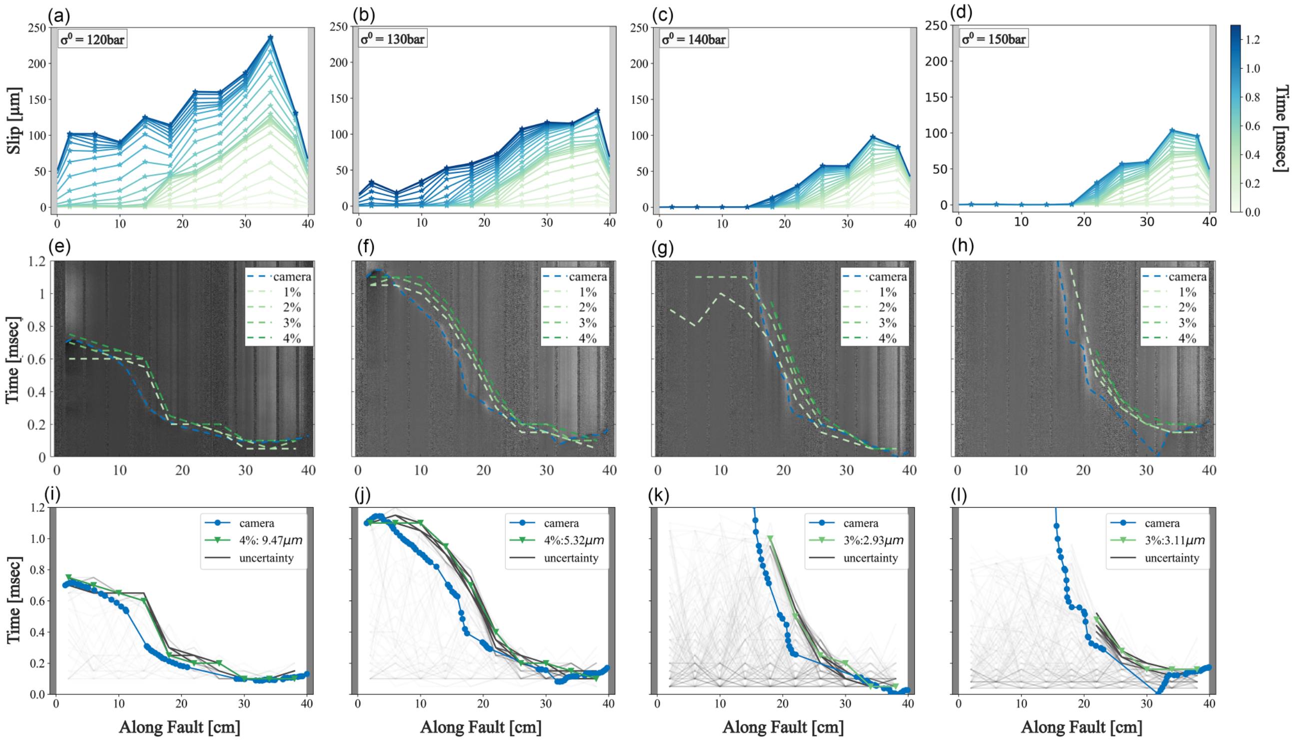

Figure 7. Quasi-static slip inversion results by using $\mathbf{G}_{\mathrm{Com}}$ (a–d) Mean posterior slip distributions for $\sigma^0 = 120$, 130, 140 and 150 bar, illustrating slip evolution over time. (e–h) Comparison of photoelastic rupture fronts (blue dashed lines) with predicted rupture fronts (green dashed lines) at varying slip thresholds, ranging from 1 per cent to 4 per cent of the maximum inverted slip value for each event. The time axis in (e–h) is aligned to the triggering time at the acoustic sensor, not to t_0 as in the other subplots. (i–l) Manually identified rupture front locations (blue points) and predicted rupture front points with associated uncertainty (grey). The uncertainty is estimated by applying the same threshold criteria in the legends to 5000 random samples drawn from the posterior distribution obtained through MCMC inversion, illustrating the variability of the solutions.

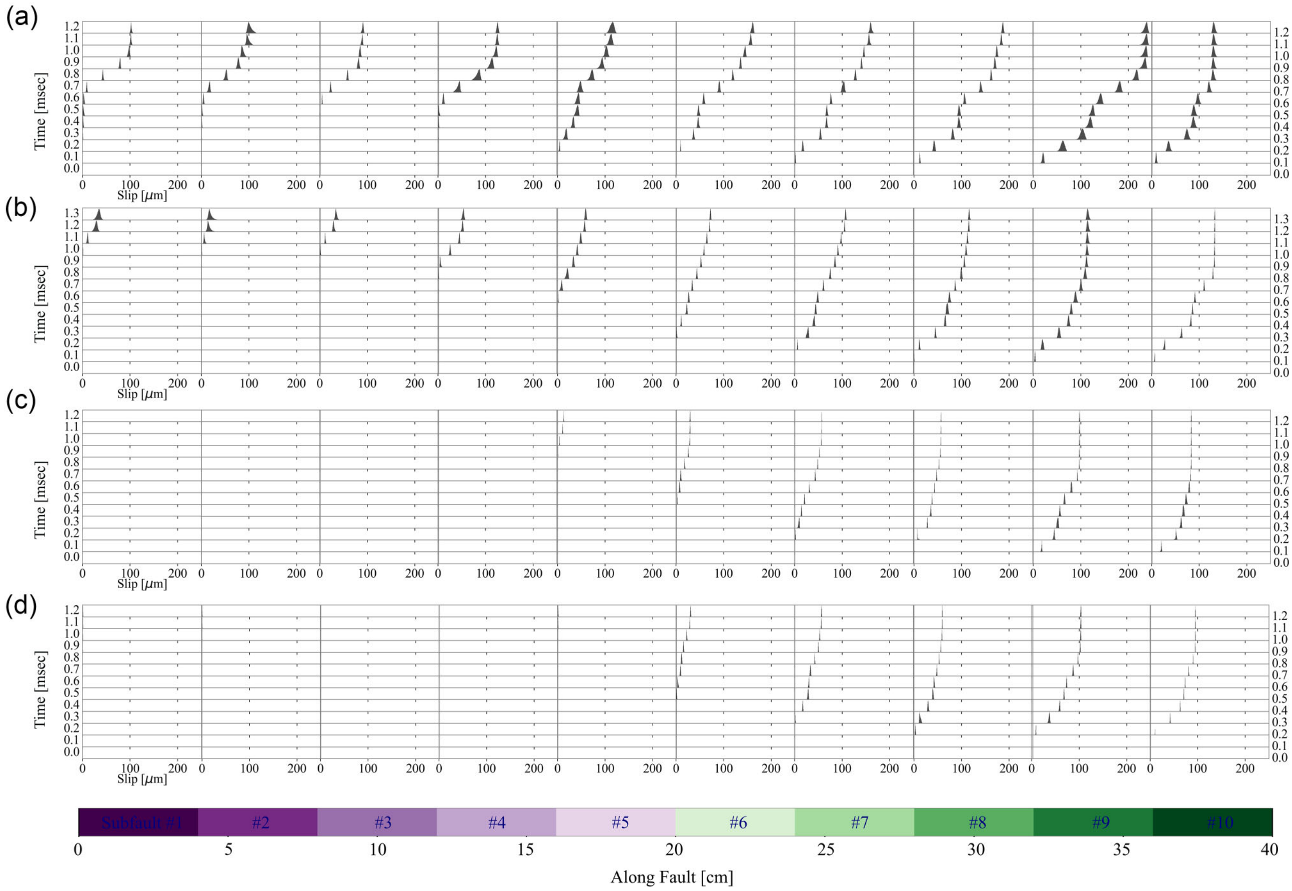

Figure 8. (Bottom) Schematic of the 40 cm fault divided into 10 subfaults (indicated in colours at the bottom). (a–d) Histograms showing the time evolution of slip in each subfault for the four experiments.

Fig. 8 presents histograms of spatiotemporal slip evolution for each experiment. In low-stress cases ($\sigma^0 = 120, 130$), the rupture traverses the whole fault, while in high-stress cases ($\sigma^0 = 140, 150$), the rupture arrests mid-fault. Slip variance diminishes with increasing σ^0 due to the constant upper slip bound of 500 μm across all events.

5 DISCUSSION

5.1 Reliability and uncertainty in static and quasi-static inversion

The non-uniqueness of slip inversions of natural earthquakes stems from limited knowledge of Earth's internal structure, simplifying assumptions in modelling, and observational noise. While synthetic tests are commonly used to explore the consequences of these limitations, they often lack realism or may introduce biases due to their reliance on idealized assumptions (I.A. Beresnev 2003). Laboratory experiments, as in our study, provide a compelling alternative by offering highly controlled environments where fault geometry and material properties are well constrained.

This study addresses a central question: can slip inversions using real laboratory data accurately recover the true slip distribution, independently recorded during experiments, when the forward model is nearly fully specified? Our results indicate that, with appropriate **GF**s, the spatiotemporal evolution of fault slip can be accurately reconstructed, even when the rupture is complex.

However, the challenge in slip inversion is not only to estimate the slip distribution but also to assess the reliability of the inferred model. Although the Bayesian framework offers a powerful means to quantify model uncertainty and evaluate model robustness, which is defined here as the stability of the posterior distribution with respect to data noise and sampling variability for a fixed forward model, it does not inherently ensure that the solution is close enough to the ground truth. In particular, the inversion using $\mathbf{G}_{\mathrm{Com}}$ reliably reproduces the true slip distribution, while the inversion using $\mathbf{G}_{\mathrm{Ok}}$ fails to do so, despite achieving a similar data fit (Figs 5a and b) and comparable uncertainty estimates (Figs 5c and d).

This discrepancy arises because the simplistic $\mathbf{G}_{\mathrm{Ok}}$, either for $W = 1$ cm or $W \gg L$, does not adequately account for the boundary conditions of the problem. As a result, it misrepresents the spatial distribution of slip and cannot reproduce the true slip pattern. In contrast, $\mathbf{G}_{\mathrm{Com}}$ incorporates realistic stress and boundary conditions, resulting in slip models that closely match independent ground-truth observations. This highlights a common but critical pitfall in inversion: inadequate forward models can yield biased yet overconfident solutions, a phenomenon we refer to as 'confidence without accuracy'. Our laboratory setting, in which forward modelling is entirely decoupled from data generation and the ground truth is independently measured, allows us to unambiguously expose this issue.

While previous studies have proposed methods to account for uncertainties in Green's functions, they have largely focused on variability in Earth material properties (Z. Duputel *et al.* 2014; M.

Hallo & F. Gallovič 2016; E. Caballero *et al.* 2023), uncertainties in fault geometry (T. Ragon *et al.* 2018) or model parametrization choices (I. Beresnev 2023). In contrast, our work specifically addresses how the treatment of geometry and boundary conditions during the computation of Green's functions can impact the inferred slip distributions. Importantly, while the geometry of the fault can be uncertain and has been rigorously explored in prior work (T. Ragon *et al.* 2018), the boundary conditions at the Earth's surface are not uncertain: the free surface is a well-constrained physical reality. However, the surface topography is often neglected or simplified in Green's function formulations. Studies show that neglecting the surface topography and the 3-D variation in elastic properties can significantly bias fault slip models, in subduction zones (C.A. Williams & L.M. Wallace 2015, 2018; L. Langer *et al.* 2019), and continental strike-slip faults (M. Marchandon *et al.* 2021). Our results demonstrate that such simplifications, especially omitting the effects of the free surface or external boundaries, can introduce systematic modelling biases. This source of epistemic uncertainty is rarely quantified or even acknowledged.

Although formally capturing this type of modelling uncertainty remains challenging, some studies have implicitly addressed it by comparing inversion results obtained under differing Green's function assumptions. For instance, J.W.C. Wong *et al.* (2024) analysed 32 published models of the 2011 Tohoku earthquake to extract robust slip features. These ensemble-based approaches offer a practical path toward quantifying uncertainty not only from data, noise or simplifications of subsurface structure, but also from the modelling choices made in Green's function construction. The effects of these choices are often excluded from formal uncertainty quantifications but can nonetheless critically influence the inversion results. Nonetheless, it remains essential to validate inversion results using independent constraints not employed in the inversion itself (S. Das & B.V. Kostrov 1990). These external benchmarks offer a practical path for assessing the physical plausibility of inferred slip models and identifying solutions that are most consistent with reality.

Since a ground truth is not available for real earthquakes, it is not possible to directly validate our results. Traditionally, discrepancies between different inversion results have been viewed as problematic, reflecting uncertainty about which solution is correct. However, especially in light of the realization that the Bayesian framework (for one inversion with a given **GF**) may not provide a fully reliable estimate of uncertainty, these differences in the literature can be reinterpreted as useful indicators. From this perspective, a variety of published slip models may not necessarily be viewed as a disadvantage. Rather, the diversity of models can serve as a transparent and practical indicator of the uncertainty and reliability of inferred results.

5.2 Implications for natural earthquakes

The spatiotemporal distribution of slip provides a kinematic description of earthquake rupture, governing the resulting stress changes, energy release and seismic moment. Consequently, uncertainties or biases in inverted slip distributions directly propagate into estimates of key source parameters and can thereby influence broader interpretations of earthquake mechanics.

In our laboratory study, we observe a pronounced dependence of the inferred seismic moment on the choice of **GF**. As shown in Fig. A4, the seismic moment predicted using $\mathbf{G}_{\mathrm{Ok}}$ is approximately three times larger than that obtained using $\mathbf{G}_{\mathrm{Com}}$, despite both inversions achieving comparable data fits and posterior uncertainty spreads. This discrepancy illustrates that modelling assumptions embedded in the **GF** can dominate the uncertainty budget, a conclusion that echoes findings by Y. Yagi & Y. Fukahata (2008), Z. Duputel *et al.* (2014) and M. Hallo & F. Gallovič (2020), who emphasized that **GF** mischaracterization often outweighs data noise as a leading source of epistemic uncertainty in finite-fault inversion.

This sensitivity to modelling uncertainties has downstream implications. Since the static stress drop is often estimated via $\Delta\sigma \approx \mathrm{M}_0/L^3$ for a circular crack of radius L, any bias in M_0 can result in an error in the stress drop for a fixed rupture length L. Such variability may account for part of the scatter in reported stress drops across studies (F. Cotton *et al.* 2013; F. Courboulex *et al.* 2016), particularly when differing simplification assumptions about medium properties are made to compute **GF**. These findings underscore the importance of carefully validating **GF** selection when comparing source parameters across different events.

Beyond scalar estimates like moment and stress drop, our inversions resolve detailed rupture kinematics. Note that the quasi-static slip inversion approach used in this study neglects elastodynamic effects such as wave propagation. Despite this simplification, it performs remarkably well in recovering rupture kinematics, including rupture fronts, velocities and arrest points, in strong agreement with independent photoelastic observations (Fig. 7). Our results suggest that the validity of the quasi-static approximation stems primarily from the nature of the laboratory setting. Ruptures propagate at sub-Rayleigh speeds, and the sensors are located in the near field, where static and low-frequency deformation dominate the measured signal. In this context, the low-frequency sensitivity of the near-field sensors used in this study is critical for double integration during data processing, which is necessary for obtaining accurate inversion results.

When our setup is scaled to natural length scales, the receiver-fault distance corresponds to a small fraction of the dominant wavelength, conditions that are commonly encountered in near-fault recordings of natural earthquakes. For our experiments, the dominant frequency of the acceleration recordings is approximately 6 kHz, which corresponds to a wavelength of about $\lambda_{\mathrm{lab}} \approx 225$ mm for the value of v_{S} in Table 2. The accelerometers are positioned at 10 mm from the fault, which corresponds to a source-to-receiver distance of about $0.04\lambda_{\mathrm{lab}}$, while the total rupture length of 400 mm represents $1.78\lambda_{\mathrm{lab}}$. This configuration is analogous to near-fault, low-frequency observations in nature. Using the same scaling, for a natural earthquake with a dominant frequency around 0.1 Hz and *S*-wave velocity between 2.5 and 4 $\mathrm{km\,s^{-1}}$, the corresponding range of wavelengths would be $\lambda_{\mathrm{nature}} = 25 - 40$ km. Thus, our experimental configuration corresponds to near-fault stations located about 1–2 km from the fault and a rupture length between 45 and 70 km. These dimensions are comparable to those of moderate-to-large earthquakes, such as the 2019 Ridgecrest, 2004 Parkfield, 2016 Amatrice, 2009 L'Aquila and 2014 Napa Valley events.

Moreover, the PMMA material used in the experiments exhibits relatively high attenuation, which naturally suppresses high-frequency wave effects. These conditions reduce the contribution of dynamic wavefields to the observed displacement, allowing the quasi-static model to capture the essential mechanics of rupture without explicitly modelling wave propagation. The high spatial resolution of the accelerometers and their proximity to the fault further enhances the effectiveness of the quasi-static inversion. As shown in Figs 7(e)–(l), even fine-scale features like deceleration zones and rupture arrests are consistently recovered. Minor timing discrepancies, especially at higher stress levels, are likely attributable to slip thresholding effects used to define rupture onset rather than

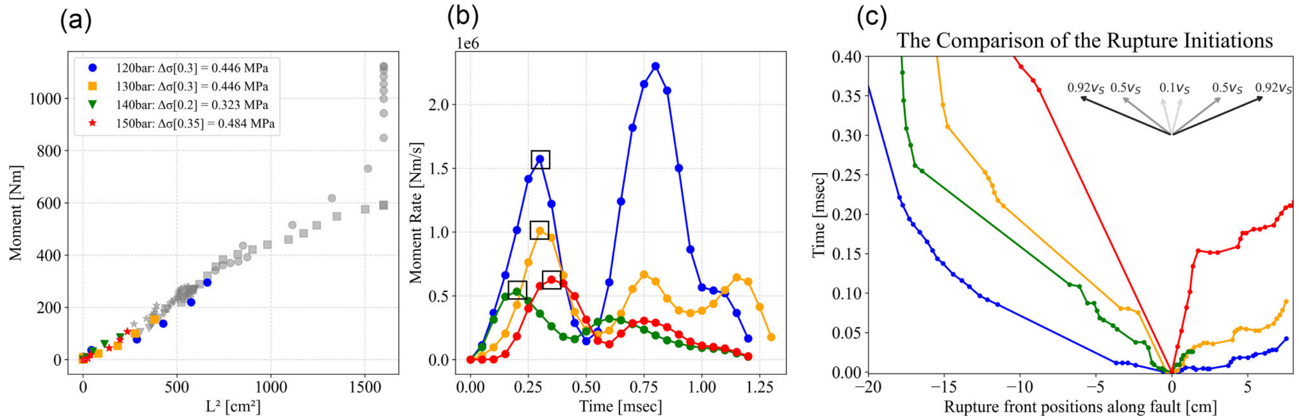

Figure 9. (a) Comparison of seismic moment versus squared rupture length L^2, derived from camera observations at each time-step. Coloured data points represent values up to the moment rate peak (highlighted in panel b), while grey symbols show subsequent evolution. Marker shapes correspond to different experimental conditions, as indicated in the legend. Stress drop values at the moment rate peak are also provided in the legend. The stress drop values, $\Delta\sigma = \mathrm{M}_0/L^2W$, computed at the time of the first moment rate peak, are also listed in the legend, where W denotes the fault width. (b) Moment rate functions for the experiments labelled in (a), with consistent colour coding. Black rectangles highlight the peak moment rate for each event. (c) True rupture front initiation along the fault (manually picked from photoelastic videograms). Time and position are relative to the rupture initiation point to allow direct comparison of rupture velocities. Example rupture velocities (0.1–0.92v_S) are annotated for reference. The absolute rupture positions and timing are shown in Fig.7

inversion errors. These results support a key assertion of S. Hartzell *et al.* (2007): dense nearfield coverage enables robust reconstructions of rupture dynamics when physically consistent assumptions are applied. However, this approximation has clear limitations. It cannot account for elastodynamic stress changes ahead of the rupture front, or any frequency-dependent phenomena. These limitations are particularly relevant for interpreting high-frequency ground motion, estimating off-fault damage or modelling ruptures approaching or outpacing the *S*-wave velocity, involving potentially strong inertia effects and strong radiated waves that carry a large portion of the rupture energy.

Finally, our inversion procedure provides a direct estimate of the seismic moment for each event (Fig. 9a), which can be used to derive the corresponding moment rate functions (Fig. 9b). Our estimate of $\dot{M}_0$ highlights that full-rupture events (e.g. $\sigma^0 = 120$, 130 bar) display longer durations and more complex, multistage moment rate evolutions. In contrast, finite-rupture events (e.g. $\sigma^0 = 140$, 150 bar) exhibit shorter and simpler moment rate profiles. Fig. 9(a) clearly shows that the stress drops at the initial peak of the moment rate, that is proportional to the slope of the L^2 versus M_0 relation, are similar across the data set. This indicates that the differences in rupture initiation in our data set are not caused by variations in stress drop. In addition, contrary to other experimental results (D. Morad *et al.* 2025), where the initial slope of the moment rate was found to scale with the final rupture size, our results show a different trend. The initial slopes of the moment-rate functions vary across our four experiments. The finite rupture events ($\sigma^0 = 140$, 150 bar) terminate at similar rupture lengths, yet their moment-rate functions initiate with different slopes. Instead, their maximum moment-rate values correlate with their similar rupture lengths. We note that the full rupture length events may be limited by the experimental setup rather than rupture dynamics, and therefore should not be overinterpreted in terms of final rupture size. The key observation in our data set is that the initial slope of four events correlates with their initial rupture velocity: as the slope decreases in Fig. 9(b), the rupture velocity decreases in Fig. 9(c).

While the limited number of experiments restricts broader generalization, the consistent relationship between the initial moment rate slope and rupture velocity is compelling. It points to a potentially scalable approach for estimating rupture kinematics using near-field displacement data alone, an especially promising avenue in natural earthquake studies where high-resolution geodetic data, dense near-field strong-motion records or distributed acoustic sensing (DAS) observations are available. The framework developed in this study opens the door to a quantitative description of the early stage of the seismic rupture in the laboratory.

6 CONCLUSION

We show that static and quasi-static inversion methods are robust tools for imaging fault slip in controlled environments with dense near-fault data coverage. Yet, the accuracy of the inversion critically depends on the assumptions embedded in the Green's function formulations, particularly those related to boundary conditions and stress heterogeneity, which differ between the Okada and COMSOL-based **GF**. When using realistic Green's functions, quasi-static inversion methods can successfully recover both the slip history and the evolution of the rupture front. We also find that the uncertainty quantification provided by Bayesian inversion is only meaningful if the forward model accurately reflects the physical system.

The findings from this laboratory study have important implications for real-world earthquake source inversion. In natural settings, key parameters for slip inversion, such as fault geometry and material properties, are poorly constrained, which limits the accuracy of any forward model. There is a circular dependence: accurate slip inversion requires a reliable **GF**, but an accurate **GF** requires knowledge of fault geometry and boundary conditions. Our results underscore the value of using the most physics-informed and site-specific **GF** available.

Our study also illustrates the strong potential of quasi-static inversion to reconstruct the rupture history from near-field displacement data alone. With increasingly dense sensor networks, including DAS and low-cost, high-rate GPS, there is a growing opportunity to track rupture evolution with high resolution, provided that the forward modelling is appropriate.

ACKNOWLEDGMENTS

F.A., B.F. and F.P. acknowledge funding from the European Union through the ERC Starting Grant HOPE (grant no. 101041966). The authors thank Julien Ambre for assistance with sensor preparation. They also thank Greg McLaskey, an anonymous reviewer and the editor for their constructive comments, which helped improve the manuscript.

DATA AVAILABILITY

The data used in this study were published by B. Fryer *et al.* (2024). The code in this study is publicly available in F. Arzu *et al.* (2025).

REFERENCES

Arzu, F., Twardzik, C., Fryer, B., Xie, Y., Ampuero, J.P. & Passelègue, F., 2025. Workflow for: static and quasi-static inversion of fault slip during laboratory earthquakes, EGU General Assembly, Vienna, Austria.

Avouac, J.P., 2015. From geodetic imaging of seismic and aseismic fault slip to dynamic modeling of the seismic cycle, *Annu. Rev. Earth planet. Sci.,* **43**(1), 233–271.

Ben-Zion, Y. & Sammis, C.G., 2003. Characterization of fault zones, *Pure appl. Geophys.,* **160**(3), 677–715.

Beresnev, I., 2023. Uncertainties in finite-fault slip inversions, part II: Fault discretization and parametrization of slip function, *Pure appl. Geophys.,* (1), 59–68.

Beresnev, I.A., 2003. Uncertainties in finite-fault slip inversions: to what extent to believe?(a critical review), *Bull. seism. Soc. Am.,* **93**(6), 2445–2458.

Caballero, E. *et al.*, 2023. Revisiting the 2015 $M_{\mathrm{w}} = 8.3$ Illapel earthquake: unveiling complex fault slip properties using Bayesian inversion, *Geophys. J. Int.,* **235**(3), 2828–2845.

Cebry, S.B.L., Sorhaindo, K. & McLaskey, G.C., 2023. Laboratory earthquake rupture interactions with a high normal stress bump, *J. geophys. Res.: Solid Earth,* **128**(11), e2023JB027297. doi:10.1029/2023JB027297.

Clévédé, E., Bouin, M.P., Bukchin, B., Mostinskiy, A. & Patau, G., 2004. New constraints on the rupture process of the 1999 August 17 Izmit earthquake deduced from estimates of stress glut rate moments, *Geophys. J. Int.,* **159**(3), 931–942.

COMSOL, Inc., 2024. *COMSOL Multiphysics® Reference Manual, Version 6.3,* Stockholm, Sweden. Available at: https://cdn.comsol.com/doc/6.3.0.290/COMSOL_ProgrammingReferenceManual.pdf

Cotton, F., Archuleta, R. & Causse, M., 2013. What is sigma of the stress drop?, *Seismol. Res. Lett.,* **84**(1), 42–48.

Courboulex, F., Vallée, M., Causse, M. & Chounet, A., 2016. Stress-drop variability of shallow earthquakes extracted from a global database of source time functions, *Seismol. Res. Lett.,* **87**(4), 912–918.

Das, S. & Kostrov, B.V., 1990. Inversion for seismic slip rate history and distribution with stabilizing constraints: application to the 1986 Andreanof islands earthquake, *J. geophys. Res.: Solid Earth,* **95**(B5), 6899–6913.

Dublanchet, P., Passelègue, F.X., Chauris, H., Gesret, A., Twardzik, C. & Nöel, C., 2024. Kinematic inversion of aseismic fault slip during the nucleation of laboratory earthquakes, *J. geophys. Res.: Solid Earth,* **129**(12). doi:10.1029/2024JB028733.

Duputel, Z., 2022. *Co-Seismic Phase: Imaging the Seismic Rupture,* ISTE Book, Chap. 2, pp. 39–77, ed. Rolandone, F., John Wiley and Sons, Ltd.

Duputel, Z., 2024. Metropolis Algorithm, GitHub repository.

Duputel, Z., Agram, P., Simons, M., Minson, S. & Beck, J., 2014. Accounting for prediction uncertainty when inferring subsurface fault slip, *J. geophys. Int.,* **197**. doi:10.1093/gji/ggt517.

Duputel, Z. *et al.*, 2015. The Iquique earthquake sequence of April 2014: Bayesian modeling accounting for prediction uncertainty, *Geophys. Res. Lett.,* **42**(19), 7949–7957.

Fryer, B., Lebihain, M., Noël, C., Paglialunga, F. & Passelègue, F., 2024. The effect of stress barriers on unconventional-singularity-driven frictional rupture, *J. Mech. Phys. Solids,* **193,** 105876. doi:10.1016/j.jmps.2024.105876.

Gallovič, F. & Ampuero, J.P., 2015. A new strategy to compare inverted rupture models exploiting the eigenstructure of the inverse problem, *Seismol. Res. Lett.,* **86,** 1679–1689.

Gallovič, F. & Zahradník, J., 2011. Toward understanding slip inversion uncertainty and artifacts: 2. singular value analysis, *J. geophys. Res.: Solid Earth,* **116**(B2). doi:10.1029/2010JB007814.

Gelman, A., Gilks, W.R. & Roberts, G.O., 1997. Weak convergence and optimal scaling of random walk Metropolis algorithms, *Ann. Appl. Probab.,* **7**(1), 110–120.

Graves, R.W. & Wald, D.J., 2001. Resolution analysis of finite fault source inversion using one- and three-dimensional green's functions: 1. strong motions, *J. geophys. Res.: Solid Earth,* **106**(B5), 8745–8766.

Hallo, M. & Gallovič, F., 2016. Fast and cheap approximation of green function uncertainty for waveform-based earthquake source inversions, *Geophys. J. Int.,* **207**(2), 1012–1029.

Hallo, M. & Gallovič, F., 2020. Bayesian self-adapting fault slip inversion with green's functions uncertainty and application on the 2016 mw7.1 kumamoto earthquake, *J. geophys. Res.: Solid Earth,* **125**(3), e2019JB018703. doi:10.1029/2019JB018703.

Hansen, B.E., 1992. Testing for parameter instability in linear models, *J. Policy Model.,* **14**(4), 517–533.

Hansen, P.C., 1998. *Rank-Deficient and Discrete Ill-Posed Problems,* Society for Industrial and Applied Mathematics.

Hartzell, S., Liu, P., Mendoza, C., Ji, C. & Larson, K.M., 2007. Stability and uncertainty of finite-fault slip inversions: application to the 2004 Parkfield, California, earthquake, *Bull. seism. Soc. Am.,* **97**(6), 1911–1934.

Hartzell, S.H. & Heaton, T.H., 1983. Inversion of strong ground motion and teleseismic waveform data for the fault rupture history of the 1979 Imperial Valley, California, earthquake, *Bull. seism. Soc. Am.,* **73**(6A), 1553–1583.

Hastings, W.K., 1970. Monte Carlo sampling methods using Markov chains and their applications, *Biometrika,* **57**(1), 97–109.

Langer, L., Gharti, H.N. & Tromp, J., 2019. Impact of topography and three-dimensional heterogeneity on coseismic deformation, *Geophys. J. Int.,* **217**(2), 866–878.

Langer, L., Beller, S., Hirakawa, E. & Tromp, J., 2022. Impact of sedimentary basins on green's functions for static slip inversion, *Geophys. J. Int.,* **232,** 569–580.

Latour, S., Schubnel, A., Nielsen, S., Madariaga, R. & Vinciguerra, S., 2013. Characterization of nucleation during laboratory earthquakes, *Geophys. Res. Lett.,* **40,** 5064–5069.

Latour, S., Passelègue, F., Paglialunga, F., Noël, C. & Ampuero, J.P., 2024. What happens when two ruptures collide?, *Geophys. Res. Lett.,* **51,** e2024GL110835 [10]. doi:10.1029/2024gl110835.

Mai, P.M. *et al.*, 2016. The earthquake-source inversion validation (SIV) project, *Seismol. Res. Lett.,* **87**(3), 690–708.

Marchandon, M., Hollingsworth, J. & Radiguet, M., 2021. Origin of the shallow slip deficit on a strike slip fault: Influence of elastic structure, topography, data coverage, and noise, *Earth planet. Sci. Lett.,* **554,** 116696. doi:10.1016/j.epsl.2020.116696.

Minson, S., Simons, M. & Beck, J., 2013. Bayesian inversion for finite fault earthquake source models I—theory and algorithm, *Geophys. J. Int.,* **194**(3), 1701–1726.

Minson, S.E. & Lee, W.H.K., 2014. Bayesian historical earthquake relocation: an example from the 1909 Taipei earthquake, *Geophys. J. Int.,* **198**(3), 1419–1430.

Minson, S.E., Murray, J.R., Langbein, J.O. & Gomberg, J.S., 2014. Real-time inversions for finite fault slip models and rupture geometry based on high-rate GPS data, *J. geophys. Res.: Solid Earth,* **119**(4), 3201–3231.

Morad, D., Gvirtzman, S., Gil, Y., Fineberg, J. & Brodsky, E., 2025. Under what circumstances is the final size of a laboratory earthquake predictable at the onset of the *P*-wave?, *Earth planet. Sci. Lett.,* **665,** 119436. doi:10.1016/j.epsl.2025.119436.

Nielsen, S., Taddeucci, J. & Vinciguerra, S., 2010. Experimental observation of stick-slip instability fronts, *Geophys. J. Int.,* **180,** 697–702.

Okada, Y., 1992. Internal deformation due to shear and tensile faults in a half-space, *Bull. seism. Soc. Am.,* **82**(2), 1018–1040.

Okamoto, T. & Takenaka, H., 2009. Waveform inversion for slip distribution of the 2006 Java Tsunami earthquake by using 2.5D finite-difference green's function, *Earth Planets Space,* **61,** e17–e20.

Olson, A.H. & Apsel, R.J., 1982. Finite faults and inverse theory with applications to the 1979 Imperial Valley earthquake, *Bull. seism. Soc. Am.,* **72**(6A), 1969–2001.

Ortega-Culaciati, F., Simons, M., Ruiz, J., Rivera, L. & Díaz-Salazar, N., 2021. An Epic Tikhonov Regularization: application to quasi-static fault slip inversion, *J. geophys. Res.: Solid Earth,* **126**(7), e2020JB021141. doi:10.1029/2020JB021141.

Paglialunga, F., Passelègue, F., Ampuero, J.P., Latour, S. & Violay, M., 2025. The role of stress distribution in seismic cycle complexity of a long laboratory fault, *Geophys. Res. Lett.,* **52**(18), e2025GL116440. doi:10.1029/2025GL116440.

Pulvirenti, F., Liu, Z., Lundgren, P., Gonzalez-Ortega, A. & Aloisi, M., 2021. New fault slip distribution for the 2010 M_w 7.2 El Mayor Cucapah earthquake based on realistic 3D finite element inversions of coseismic displacements using space geodetic data, *J. geophys. Res.: Solid Earth,* **126**(1), e2020JB020016. doi:10.1029/2020JB020016.

Ragon, T., Sladen, A. & Simons, M., 2018. Accounting for uncertain fault geometry in earthquake source inversions–I: theory and simplified application, *Geophys. J. Int.,* **214**(2), 1174–1190.

Romanet, P., Bhat, H.S., Jolivet, R. & Madariaga, R., 2018. Fast and slow slip events emerge due to fault geometrical complexity, *Geophys. Res. Lett.,* **45**(10), 4809–4819.

Rosakis, A., Samudrala, O. & Coker, D., 1999. Cracks faster than the shear wave speed, *Science,* **284,** 1337–1340.

Scholz, C., 2002. *The Mechanics of Earthquake Faulting,* Cambridge Univ. Press.

Schubnel, A., Nielsen, S., Taddeucci, J., Vinciguerra, S. & Rao, S., 2011. Photo-acoustic study of subshear and supershear ruptures in the laboratory, *Earth planet. Sci. Lett.,* **308,** 424–432.

Schwarz, G., 1978. Estimating the dimension of a model, *Ann. Stat.,* **6,** 461–464.

Sibson, R., 1989. Earthquake faulting as a structural process, *J. Struct. Geol.,* **11,** 1–14.

Tarantola, A., 2005. *Inverse Problem Theory and Methods for Model Parameter Estimation,* vol. **xii,** SIAM. Available at: https://www.geologie.ens.fr/~jolivet/Research_files/Tarantola.pdf

Tarantola, A. & Valette, B., 1982. Generalized nonlinear inverse problems solved using the least squares criterion, *Rev. Geophys.,* **20**(2), 219–232.

Twardzik, C., Duputel, Z., Jolivet, R., Klein, E. & Rebischung, P., 2022. Bayesian inference on the initiation phase of the 2014 Iquique, Chile, earthquake, *Earth planet. Sci. Lett.,* **600,** 117835. doi:10.1016/j.epsl.2022.117835.

Williams, C.A. & Wallace, L.M., 2015. Effects of material property variations on slip estimates for subduction interface slow-slip events, *Geophys. Res. Lett.,* **42**(4), 1113–1121.

Williams, C.A. & Wallace, L.M., 2018. The impact of realistic elastic properties on inversions of shallow subduction interface slow slip events using seafloor geodetic data, *Geophys. Res. Lett.,* **45**(15), 7462–7470.

Wong, J.W.C., Fan, W. & Gabriel, A.A., 2024. A quantitative comparison and validation of finite-fault models: the 2011 Tohoku-Oki earthquake, *J. geophys. Res.: Solid Earth,* **129**(10), e2024JB029212. doi:10.1029/2024JB029212.

Yagi, Y. & Fukahata, Y., 2008. Importance of covariance components in inversion analyses of densely sampled observed data: an application to waveform data inversion for seismic source processes, *Geophys. J. Int.,* **175**(1), 215–221.

APPENDIX A:

A1 GF calculation in comsol

The geometry is partitioned into 174392 domain elements, with refinement around the source and sensors (within 1 cm of the fault plane) to 0.0015 m. The 4 blocks and 4 cylinders (shown in blue in Fig. A1), used to transfer the loading and smooth the stress field, are modelled using steel, which is elastic and characterized by a Young's modulus of 2e11 Pa and a Poisson's ratio of 0.27. The green regions indicate areas where loading is applied (with uniform pressure, P_{N_1} and $P_{N_2} = 120$ bar, $P_{N_3} = 0$ and $P_S = 190$ bar, as in Table 3). The transparent red regions mark surfaces with roller boundary conditions (i.e. displacement in the surface normal direction is fixed at zero, while displacement in the surface-parallel direction is free). All the other surfaces are treated as free surfaces. We utilize a thin layer module (spring material) (F. Pulvirenti *et al.* 2021) to model the dislocation on the subfaults.

A2 Model parametrization

To determine the granularity of the space-time discretization, we analysed the Bayesian Information Criterion (BIC), defined as:

$$\mathrm{BIC} = k \ln(n) - 2 \ln(\widehat{L}) \,, \tag{A1}$$

where k is the number of unknown parameters, n is the number of data points and $\widehat{L}$ is the maximum-likelihood value within the model space (G. Schwarz 1978).

We first determine the spatial discretization of the static-slip inversion. We run multiple source inversions, with an increasing number of subfaults ranging from 4 to 25. We set the subfault width equal to the sample width; thus, we restrict the inversion to slip fluctuations along strike but not along dip. After each inversion, we calculate the average likelihood. Using the L-curve method (B.E. Hansen 1992), we find that 10 subfaults offer the best compromise between data fitting and model complexity. Each of these 10 subfaults has a length of 4 cm and a width of 1 cm (Fig. 4).

For the quasi-static slip inversion, we keep the same spatial discretization of 10 subfaults. Therefore, we only run the BIC analysis to determine the number of temporal basis functions that parametrize the slip rate of each subfault. Based on the BIC analysis, we find an optimal value of 8 temporal basis functions per subfault (Fig. A2).

A3 Model covariance matrices

Apart from the inversion process itself, it is possible to analytically calculate the model covariance matrix for a given linear forward problem $\mathbf{d} = \mathbf{G}\mathbf{m}$ assuming Gaussian noise in the data without any prior information, such that $\mathrm{C_m} = (\mathbf{G}^T \mathrm{C_d}^{-1} \mathbf{G})^{-1}$, where $\mathrm{C_d}$ is the data covariance matrix (A. Tarantola 2005).

A4 The uncertainty of predicted seismic moment

The seismic moment for the experiment with $\sigma^0 = 140$ bar is calculated as follows:

$$\mathrm{M_0}(t) = \sum_{i}^{10} \mu L_i W_i \mathbf{m}_i(t), \tag{A2}$$

where L_i, W_i and $\mathbf{m}_i$ are the length, width and inverted total slip amount of the subfault for the ith subfault. The time variable t is relevant only for quasi-static results. Fig. A4 presents the seismic moment computed from static inversion results, that is, the total coseismic slip values for the event with $\sigma^0 = 140$ bar.

A5 Moment rate function

We compute $\dot{\mathrm{M}}_0(t)$ numerically by differentiating the cumulative moment $\mathrm{M_0}(t)$ in eq. (A2) obtained from the slip histories of the subfaults.

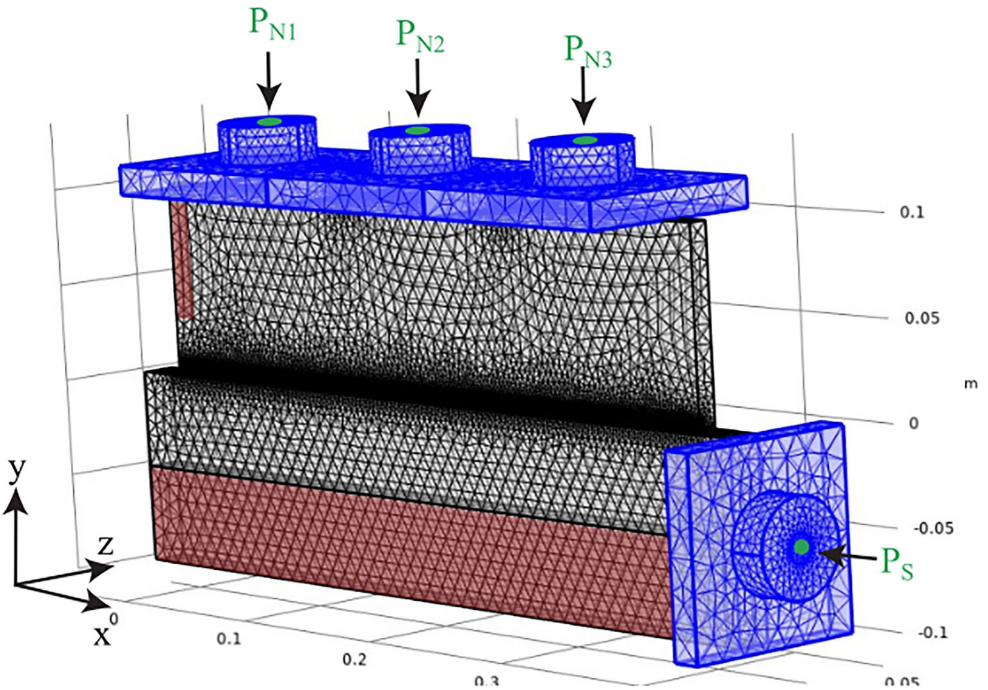

Figure A1. The geometry and meshgrid for finite element method in Comsol.

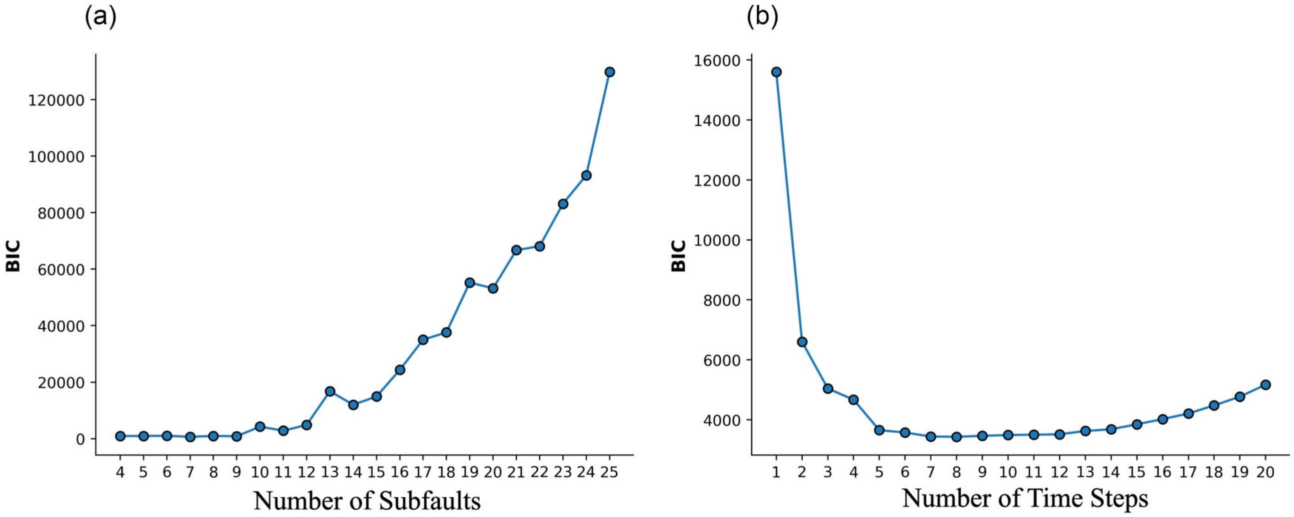

Figure A2. BIC analysis for number of subfaults (a) and number of time-steps (b).

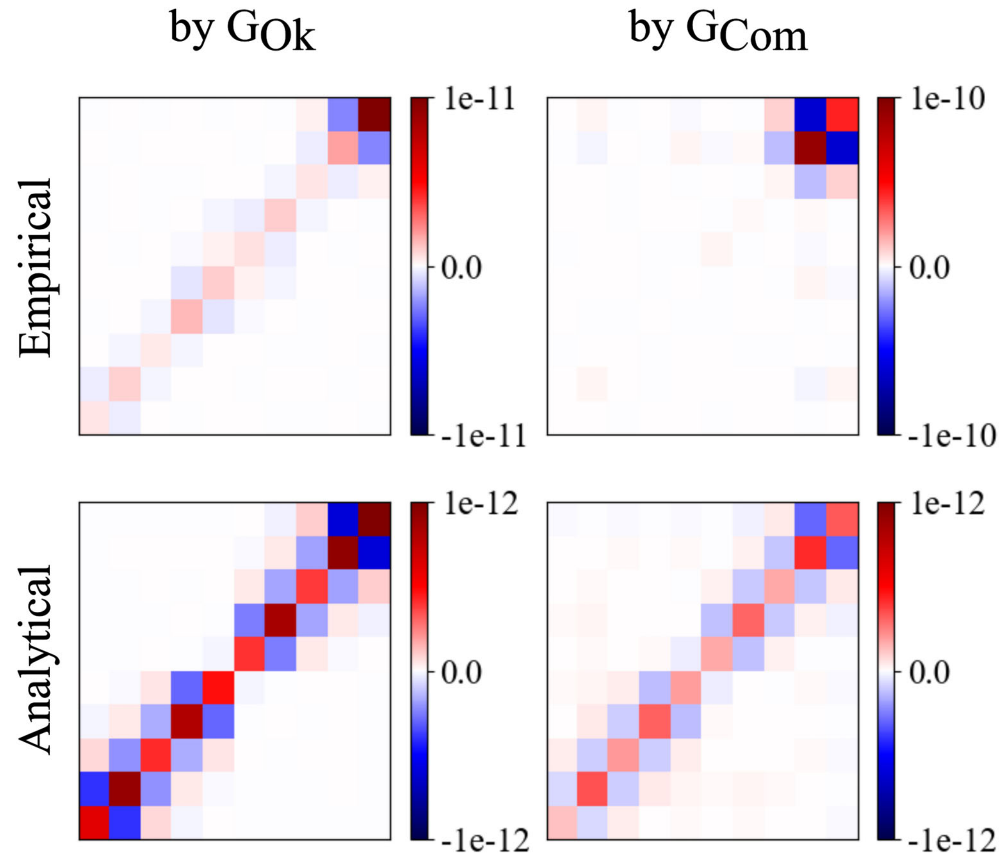

Figure A3. The comparison of empirical model covariance matrices from the posterior (for Okada and Comsol, respectively) and analytical covariance matrices for a Gaussian linear model without prior information (A. Tarantola 2005).

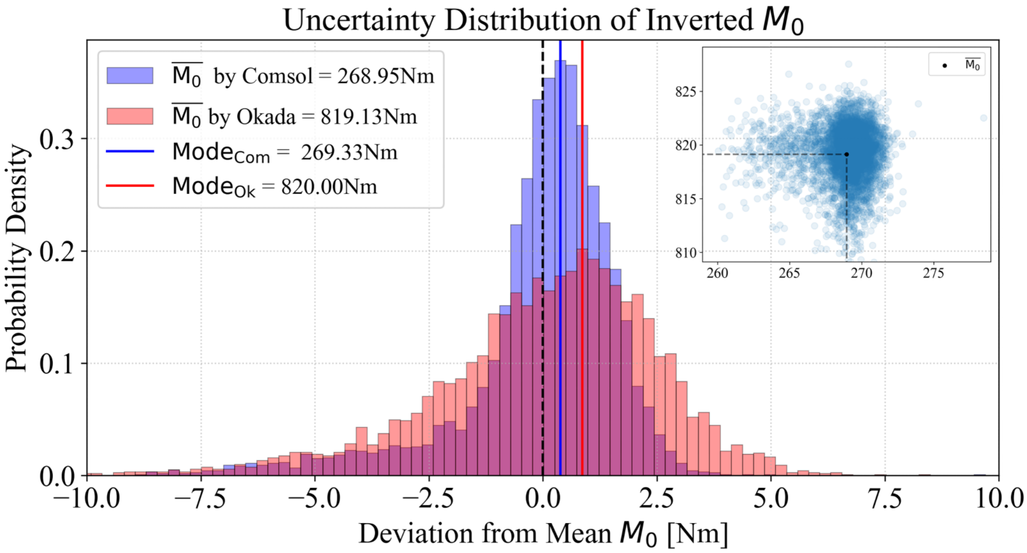

Figure A4. Marginalized 1-D posterior probability distributions of seismic moment M_0 centred at their respective means for both $\mathbf{G}_{\mathrm{Ok}}$ and $\mathbf{G}_{\mathrm{Com}}$ inversion results.